HHS Public Access

Author manuscript

J Neural Eng. Author manuscript; available in PMC 2024 June 15.

Published in final edited form as:

J Neural Eng. ; 20(3): . doi:10.1088/1741-2552/acda64.

Validated Computational Models Predict Vagus Nerve Stimulation Thresholds in Preclinical Animals and Humans

Eric D. Musselman[1], **Nicole A. Pelot**[1,*], **Warren M. Grill**[1,2,3,4,*]

[1]Department of Biomedical Engineering, Duke University, Durham, NC, United States of America

[2]Department of Electrical and Computer Engineering, Duke University, Durham, NC, United States of America

[3]Department of Neurobiology, Duke University, Durham, NC, United States of America

[4]Department of Neurosurgery, Duke University, Durham, NC, United States of America

Abstract

Objective—We demonstrated how ASCENT (Automated Simulations to Characterize Electrical Nerve Thresholds), a recently published open-source software for modeling stimulation of peripheral nerves, can be applied to simulate accurately nerve responses to electrical stimulation.

Approach—We simulated vagus nerve stimulation (VNS) for humans, pigs, and rats. We informed our models using histology from sample-specific or representative nerves, device design features (i.e., cuff, waveform), published material and tissue conductivities, and realistic fiber models.

Main Results—Despite large differences in nerve size, cuff geometry, and stimulation waveform, the models predicted accurate activation thresholds across species and myelinated fiber types. However, our C fiber model thresholds overestimated thresholds across pulse widths, suggesting that improved models of unmyelinated nerve fibers are needed.

Our models of human VNS yielded accurate thresholds to activate laryngeal motor fibers and captured the inter-individual variability for both acute and chronic implants. For B fibers, our small-diameter fiber model underestimated threshold and saturation for pulse widths >0.25 ms.

Our models of pig VNS consistently captured the range of in vivo thresholds across all measured nerve and physiological responses (i.e., heart rate, Aδ/B fibers, Aγ fibers, EMG, and Aα fibers).

In rats, our smallest diameter myelinated fibers accurately predicted fast fiber thresholds across short and intermediate pulse widths; slow unmyelinated fiber thresholds overestimated thresholds across shorter pulse widths, but there was overlap for pulse widths >0.3 ms.

Significance—We elevated standards for models of peripheral nerve stimulation in populations of models across species, which enabled us to model accurately nerve responses, demonstrate

warren.grill@duke.edu .

*These authors contributed equally to this work.

Conflicts of Interest

None of the authors have conflicts of interest.

that individual-specific differences in nerve morphology produce variability in neural and physiological responses, and predict mechanisms of VNS therapeutic and side effects.

Keywords

vagus nerve stimulation; neural computational modeling; peripheral nerve stimulation

Introduction

Despite promising preclinical studies of vagus nerve stimulation (VNS) to treat a range of diseases, therapies often fail to translate to successful clinical outcomes. To accelerate translation of novel applications of VNS to the clinic, quantitatively validated models are needed for populations of individuals across species. Prior modeling studies greatly enhanced our understanding of how nerves respond to electrical stimulation, but, with few exceptions, validation efforts were limited to matching only trends or phenomena to experimental data. Validated models of VNS enable model-based design of electrode geometries and stimulation waveforms to maximize therapeutic benefits, minimize side effects, and tailor individual-specific stimulation parameters, thereby overcoming challenges associated with translation.

Our models advance the state of the art for computational modeling of peripheral nerve stimulation by representing populations of individual-specific nerves, implementing accurate cuff geometries, using best practices for modeling electrical stimulation with current sources in COMSOL (Pelot et al., 2018), using accurate material conductivities (Pelot et al., 2017, 2019), using a rigorous process for selecting fiber diameters, conducting model convergence analyses on thresholds (Howell & Grill, 2014), and making quantitative comparisons to in vivo data.

We modeled populations of human and pig vagus nerves based on histology, and for a cohort of the pigs, we modeled the histology for the nerves of the animals from which the in vivo data were collected. Many previous studies modeled peripheral nerve stimulation using generalized nerve morphologies (Aristovich et al., 2021; Arle et al., 2016; Bucksot et al., 2021; Deurloo et al., 1998, 2000; Eiber et al., 2021; Fang & Mortimer, 1991; Frieswijk et al., 1998; Lazorchak et al., 2022; Pelot et al., 2019, 2017; Sweeney et al., 1990), and fewer included individual-specific representations of nerve morphology (Blanz et al., 2023; Dali et al., 2018; Helmers et al., 2012; Musselman et al., 2021; Raspopovic et al., 2012). However, we are the first to study VNS responses across populations of individuals, which allows us to capture the variance in thresholds arising from differences in nerve morphology.

We modeled accurate and detailed cuff electrode geometries to match the designs used experimentally for each of our sources of clinical and preclinical VNS validation data. Prior VNS modeling studies also took considerable effort to represent accurately the cuff used in preclinical (Blanz et al., 2023; Lazorchak et al., 2022; Musselman et al., 2021) and clinical studies (Helmers et al., 2012). Further, some studies used model-based design to select novel VNS cuff geometries to test in vivo (Aristovich et al., 2021; Dali et al., 2018).

Previous VNS modeling studies did not report quantitative matches between model thresholds and signals recorded in vivo. Herein, we validated modeled activation thresholds for human (n = 9), pig (n = 20), and rat (n = 1) VNS. Models were implemented in the ASCENT (Automated Simulations to Characterize Electrical Nerve Thresholds) platform, an open-source tool that enables standardized and shareable models of peripheral nerve stimulation (Musselman et al., 2021). Our results demonstrate the functionality of ASCENT to implement detailed models of nerve stimulation and make accurate predictions of thresholds for a wide range of nerve geometries (~0.2–4 mm diameter, 1–76 fascicles), cuffs used clinically and in preclinical studies (LivaNova helical and Micro-Leads Neuro cuffs), myelinated and unmyelinated fibers, waveform pulse widths, and nerve interfaces for both acute and chronic implants.

Methods

Overview of Models of VNS

We used ASCENT v1.1.1 (Musselman et al., 2021) to implement anatomically-realistic computational models of VNS. Using segmented histology from (Pelot et al., 2020c), we defined the nerve cross section for 9 human (Pelot et al., 2020a) and 12 pig (Pelot et al., 2020b) mid-cervical vagus nerves. We modeled an additional 8 pigs from (Nicolai et al., 2020; Settell et al., 2023) for which corresponding in vivo thresholds were published (Nicolai et al., 2021). Lastly, we modeled a generalized rat vagus nerve based on published morphology (Pelot et al., 2020c) using the nerve morphology generator in ASCENT. We compared model responses to data from experiments in humans (Ardesch et al., 2010; Banzett et al., 1999; Bouckaert et al., 2022; Pascual, 2015; Premchand et al., 2014; Vespa et al., 2019; Zannad et al., 2015), pigs (Nicolai et al., 2020, 2021), and rats (Pelot & Grill, 2020). The complete dataset, model parameters (including cuff geometries and segmented histology images), and ASCENT inputs are provided in the associated published dataset (Musselman et al., 2023). All data analyses and plotting used Python 3.7 (Van Rossum & Drake, 2009).

We dilated human and pig nerve geometries to correct for 20% tissue shrinkage during histological processing (Boyd & Kalu, 1979; Friede & Samorajski, 1967; Hursh, 1939; Stickland, 1975). Using the physics-based deformation process in ASCENT, we reshaped the human and pig nerve segmentations to match the circular shape of the cuff, maintaining nerve cross-sectional area and fascicle shapes; the algorithm maintained at least 10 μm separation between adjacent fascicles and from each fascicle to the nerve boundary. For all models, we extruded the nerve cross section along the length of the nerve to create a 3D model.

Using COMSOL v5.6 (COMSOL Inc., Burlington, MA, USA), we implemented finite element models (FEMs) to solve for the electric potentials in each vagus nerve in response to current delivered through a cuff electrode. We instrumented each nerve with the cuff geometries that were used experimentally, including modeling a silicone electrode substrate and each electrode contact as a thin platinum domain containing a point current source (Callister & Rethwisch, 2012; de Podesta et al., 1996; Pelot et al., 2018) (Table 1, Figure 1(a),(e),(g), Figure 4(a)). We placed the cuff electrode halfway along the nerve length. We

assigned an electrical conductivity to each neural tissue type (Table 1), and the cylindrical domain surrounding the nerve and cuff electrode was skeletal muscle to mimic the cervical vagus neck region. We grounded the outer boundaries of the model to represent an implanted pulse generator or subdermal needle serving as electrical ground.

In a representative model for each species, we conducted convergence analysis to verify that the parameters of the FEM did not affect simulation results while reducing computational demands. Specifically, we verified that the surrounding cylindrical medium of our FEM was large enough (i.e., length, diameter) and the mesh was fine enough such that activation thresholds did not change by more than 2% as compared to a larger model with a finer mesh resolution (Howell et al., 2014). Additionally, we ensured that the nerve length resulted in a sufficient number of nodes of Ranvier such that the largest fibers did not exhibit end excitation. The cylindrical domain lengths were 50 mm for humans, 25 mm for pigs, and 12.5 mm for rats; the cylindrical domain diameters were 10 mm for humans, 10 mm for pigs, and 6 mm for rats. The converged models had ~10,000,000, ~20,000,000, and 660,801 tetrahedral elements for humans, pigs, and rats, respectively.

We computed electric potentials in COMSOL using conjugate gradients to solve Laplace's equation with second order solution and shape geometry functions. We solved the model for each contact independently delivering 1 mA while the remaining current sources were set to 0 mA, which defined our solution bases; we scaled and summed the contributions of each contact to determine extracellular potentials along the trajectory of each fiber. ASCENT applied the potentials as a time-varying signal to multicompartment, cable models of mammalian myelinated and unmyelinated fibers in NEURON v7.6 (Hines & Carnevale, 1997). We used a time step of 1 μs with backward Euler integration and delivered the stimulation pulse after one millisecond. We checked for action potential propagation at 90% of fiber length (i.e., the side opposite of the cathode during the primary phase of the waveform) for thresholds. We detected an action potential as transmembrane potential crossing −30 mV with a rising edge. Using a bisection search algorithm, we determined activation thresholds with a 1% tolerance. To check for bidirectional propagation at threshold, we recorded times during the simulation at which action potentials were detected at either end of the fiber (i.e., nodes of Ranvier nearest 10% and 90% fiber length).

Clinical and Preclinical Data for Model Validation

Humans—We compared modeled activation thresholds for human VNS with different fiber diameters to published clinical recordings of laryngeal EMG responses and changes in heart rate. We included studies that used the standard cuff for treatment of epilepsy (helical, bipolar; LivaNova PLC, London, UK) and that reported time post-implant (i.e., to infer whether the cuff would be encapsulated in scar tissue). All human data reported pulse width and stimulation amplitude, but not the precise waveform shapes. Across all sources we used to validate our models, except for 3/8 patients in (Ardesch et al., 2010), the LivaNova pulse generator delivered a biphasic waveform with a primary phase rectangular pulse followed by a passive recharge phase; the amplitude and time constant of LivaNova's passive recharge phase have not been disclosed. Three patients in (Ardesch et al., 2010) were stimulated with

UT VN stimulator (University of Twente, The Netherlands), but the details of the waveform shape were not reported.

We compared modeled Aα thresholds to laryngeal EMG thresholds from three VNS studies (Ardesch et al., 2010; Bouckaert et al., 2022; Vespa et al., 2019), and we compared modeled B fiber thresholds to two studies where VNS induced bradycardia in some patients (Pascual, 2015; Premchand et al., 2014) and two studies where VNS did not evoke bradycardia in any patients (Banzett et al., 1999; Zannad et al., 2015). Brief overviews of these clinical studies, as well as our methods for extracting data from the original sources, are provided in Appendix 1 for laryngeal EMG and in Appendix 2 for bradycardia.

Pigs—We compared our models of pig VNS to in vivo recordings in 8 anesthetized pigs (1.5–3% isoflurane in air, 5 μg/kg i.v. bolus of fentanyl followed by 5 μg/kg/hr) published in (Nicolai et al., 2020, 2021; Settell et al., 2023). The in vivo experiments measured compound action potentials (CAPs), laryngeal EMG, and heart rate. We used WebPlotDigitizer (Rohatgi, 2022) to extract the stimulation thresholds from Figure 6(a) in (Nicolai et al., 2020); we included data points for both the left and right vagus nerves, which we reproduced in Figure 2. For each animal, we determined in vivo threshold resolution from the amplitudes tested in all animals (0.1, 0.2, 0.3, 0.4, 0.5, 0.75, 1, 2, 2.5, 3 mA) (Nicolai et al., 2020) and the amplitudes listed in performances.xlsx from (Nicolai et al., 2021), which reports additional amplitudes tested in each animal.

Rats—In vivo strength-duration data from 9 anesthetized rats (1.2 g/kg urethane SQ, with supplemental doses up to 0.4 g/kg) are from Figure B2 in Appendix B of (Pelot & Grill, 2020), which shows CAP data for “slow” (0.5–2 m/s) and “fast” (2–10 m/s) fibers.

Fiber Model Selection

We used a rigorous approach to select modeled fiber diameters to compare to experimental neural and physiological response thresholds (Table 2). For experiments that recorded CAPs and analyzed their CVs, we selected fiber models with matched CVs. We also used latencies of VNS-evoked laryngeal EMG responses from (Ardesch et al., 2010) to estimate fiber CV using methods published in (Vespa et al., 2019) (Appendix 3). If experimental CV data were not available, we matched fiber models to published distributions of fiber diameters for vagus nerves of the same species. Appendix 3 provides detailed methods for selecting fiber diameters.

For myelinated fibers, we used the ASCENT implementation of the MRG (McIntyre-Richardson-Grill) model of myelinated mammalian peripheral nerve fibers. We interpolated the dimensions of each ultrastructural compartment across fiber diameters (McIntyre et al., 2002, 2004; Musselman et al., 2021) and selected fiber diameters to the nearest 0.5 μm to match a target CV (Appendix 4).

For C fibers, we used the “parent” section of the Tigerholm model of unmyelinated mammalian peripheral nerve fibers with diameters selected to the nearest 0.1 μm to match a target CV (Tigerholm et al., 2014).

In models of human and pig VNS, we aligned the middle node of Ranvier at the longitudinal center of the model in all simulations; our simulations showed that longitudinal placement of nodes did not affect fiber activation thresholds in these nerves (data not shown). However, in the model of rat VNS, where the electrode-fiber distances were much shorter, the position of central node of Ranvier was randomly shifted within half an internodal length in either direction.

Quantifying Model Responses

For the multifascicular human and pig vagus nerves, we simulated one fiber at the centroid of each fascicle because, for a given fiber diameter, thresholds vary little within fascicles (Pelot et al., 2017). Another VNS modeling study also showed that thresholds for a given fiber diameter vary little for fibers at different locations within a fascicle relative to fiber locations across fascicles (see Figure 12 in the Supplementary Materials of (Davis et al., 2023)). For the monofascicular rat vagus nerve, we simulated 13 fibers placed in a “wheel” pattern, which contains a fiber at the centroid and six radial spokes with two fibers each. We simulated all relevant fiber diameters (Table 2) at each fiber location.

In our human and pig models, we defined onset and saturation by the lowest and highest threshold fibers in the nerve, respectively, across fiber locations for a given fiber diameter. For humans, we compared the range of modeled Aα fiber thresholds to experimental EMG data for onset (Ardesch et al., 2010; Bouckaert et al., 2022; Vespa et al., 2019) and saturation thresholds (Bouckaert et al., 2022; Vespa et al., 2019), and we compared the range of modeled B fiber thresholds to absence or incidence of bradycardia (Banzett et al., 1999; Pascual, 2015; Premchand et al., 2014; Zannad et al., 2015). For pigs, we compared the range of modeled fiber thresholds (Aα, Aγ, Aδ/B) to onset of the neural response (electroneurogram; ENG) or physiological responses (laryngeal EMG, bradycardia) (Nicolai et al., 2020). In our rat model, we compared the threshold for the 50^{th} percentile of modeled “fast” myelinated and “slow” unmyelinated fibers to the threshold activating 50% of the area-under-the-curve of the maximum CAP in the corresponding CV range from the strength-duration data in (Pelot & Grill, 2020).

Models of Human VNS

We used segmented cross sections of mid-cervical vagus nerve samples from nine embalmed human cadavers (Pelot et al., 2020a) (Figure 1(b)). For fascicles with multiple endoneurium bundles (i.e., “peanut” fascicles that have one or more intrafascicular perineurial septa), we meshed the perineurium as a conductive domain with finite thickness and conductivity σ_{peri} (S/m) (Table 1); otherwise, we represented the perineurium using a surface impedance $(R_m,\ \Omega \cdot m^2)$, where the thickness $(thk_{peri},\ m)$ was defined by the difference in radii of the effective circular diameters for the outer and inner perineurium boundaries.

$$R_m = \frac{thk_{peri}}{\sigma_{peri}} \tag{1}$$

We created FEMs of acute and chronic human VNS for each of the 9 nerve samples. We instrumented all nerves with the LivaNova bipolar helical cuff electrode based on CAD files

from LivaNova (Figure 1(a)), as used in the clinical data against which we validated the models. For the models of acute VNS (Ardesch et al., 2010; Bouckaert et al., 2022), we modeled a uniform 100 μm thick saline layer on all surfaces of the cuff electrode—i.e., between the cuff and the nerve and between the cuff and the muscle (Figure 1(e)); a single saline domain extended to surround both helices of the cuff. For models of chronic VNS (Bouckaert et al., 2022; Vespa et al., 2019), we added an encapsulation tissue layer to the model. Post-mortem histology of a patient with VNS showed ~100 μm of encapsulation tissue between the nerve and cuff (Arle et al., 2016), but a wide range of encapsulation thicknesses are reported (e.g., 35 to 300 μm thick in cat sciatic nerve stimulation with a self-sizing spiral cuff electrode (Grill & Mortimer, 1994; Haberler et al., 2000; Moss et al., 2004; Romero et al., 2001)). Based on a video of a VNS explant surgery (Aalbers et al., 2015), we modeled a uniform 100 μm thick saline layer on all surfaces of the cuff electrode, as in the acute model, as well as a layer of encapsulation tissue that was 250 μm thick radially around the saline (Figure 1(g)) and extended longitudinally for an additional half cuff length (~2 mm) in both longitudinal directions.

We modeled the LivaNova cuff to expand from its resting inner diameter of 1.98 mm (“2 mm”) or 3 mm to accommodate the diameter of the nerves; the effective circular diameter of the nerves after shrinkage correction were 1.28–3.18 mm (median: 2.35 mm). If the post-shrinkage-correction nerve diameter plus 100 μm saline and 250 μm encapsulation layers was <3 mm, we used the 2 mm-diameter LivaNova cuff; otherwise, we used the 3 mm-diameter LivaNova cuff. (Bouckaert et al., 2022; Vespa et al., 2019) did not report if they used the 2 mm or 3 mm diameter cuffs in their studies, but the data from (Ardesch et al., 2010) included patients implanted with the 2 mm ($n = 5$) and 3 mm ($n = 1$) diameter cuffs.

We used a biphasic symmetric rectangular pulse with no delay between phases and pulse widths from 0.05 to 1 ms per phase. The LivaNova implanted pulse generator has a passive secondary recharge phase that we approximated to be rectangular.

Models of Pig VNS

We used histology from 20 pig cervical vagus nerves stained with Masson’s trichrome (Nicolai et al., 2020, 2021; Pelot et al., 2020b, 2020c; Settell et al., 2023) to define the nerve geometry. For 8 of the pigs, we could compare directly to their published in vivo neural and physiological responses (Nicolai et al., 2020, 2021; Settell et al., 2023). Using Nikon NIS-Elements Ar software (v5.02.01, Build 1270, Nikon Instruments Inc.), we segmented the perineurium and nerve outline to define the cross sections in ASCENT. We modeled the perineurium as a surface impedance (Pelot et al., 2019; Weerasuriya et al., 1984) (Table 1, Eq. 1) calculated with thickness (thk_{peri}, μm) based on the effective circular diameter of the fascicle (d_{fasc}, μm) (Pelot et al., 2020c):

$$thk_{peri} = 0.02547 * d_{fasc} + 3.440 \quad (2)$$

As in humans, for models based on the histology for 12 pigs from (Pelot et al., 2020c), we modeled the LivaNova cuff to expand from its resting inner diameter of 1.98 mm (“2 mm”)

or 3 mm to accommodate the diameter of the nerves; the nerve diameters after shrinkage correction were 2.28–3.39 mm (median: 2.72 mm). If the post-shrinkage-correction nerve diameter plus 100 μm saline layer was <3 mm, we used the 2 mm-diameter LivaNova cuff; otherwise, we used the 3 mm diameter LivaNova cuff. For models based on the histology for 8 pigs from (Nicolai et al., 2020; Settell et al., 2023), we used the 2 mm diameter LivaNova cuff as used in vivo; the nerve diameters after shrinkage correction were 2.45–3.95 mm (median: 3.65 mm).

We used a 0.2 ms/phase biphasic symmetric rectangular pulse with no inter-phase delay to match the waveform used in vivo (Nicolai et al., 2020).

Models of Rat VNS

We modeled a monofascicular circular rat vagus nerve with a diameter of 235 μm based on published data (Pelot et al., 2020c) using the ASCENT nerve morphology generator (Figure 4(a)). We modeled the perineurium as a surface impedance (Pelot et al., 2019; Weerasuriya et al., 1984) (Eq. 1) with thickness ($thk_{peri},\ \mu m$) based on the effective circular diameter of the fascicle ($d_{fasc},\ \mu m$) (Pelot et al., 2020c):

$$thk_{peri} = 0.01292 * d_{fasc} + 1.367 \quad (3)$$

We modeled a 300 μm diameter bipolar Micro-Leads cuff electrode (Somerville, MA, USA) to match experimental data from (Pelot & Grill, 2020) (Figure 4(a)). We modeled a uniform 10 μm thick saline layer on all surfaces of the cuff electrode since the nerve and cuff electrode are ~10x smaller in rats than pigs or humans.

We used a biphasic symmetric rectangular pulse with no delay between phases and pulse widths of 0.02 to 2 ms per phase to match the waveforms used in vivo (Pelot & Grill, 2020).

Results

We compared thresholds from computational models of human, pig, and rat VNS to clinical and preclinical data. The models matched well the experimental thresholds of activation for myelinated fibers, but overestimated activation thresholds for C fibers, especially at shorter pulse widths. Additionally, the populations of histology-based human and pig models reproduced the ranges of activation thresholds observed in vivo and clinically, thereby demonstrating that individual differences in nerve morphology contribute to within-species differences in nerve responses. Encapsulation tissue increased thresholds in our human models, but not to the amplitudes tolerated in the clinic, which suggests that mechanisms beyond encapsulation contribute to the increase over time in tolerable stimulation amplitudes. Lastly, action potentials propagated bidirectionally away from the electrode for all simulations at activation threshold amplitudes, and we did not observe instances of conduction block at these intensities.

Human VNS

To compare modeled Aα activation thresholds to clinical EMG data in acutely and chronically implanted patients (Ardesch et al., 2010; Bouckaert et al., 2022; Vespa et al., 2019), we simulated strength-duration data for the fastest and slowest Aα fibers recorded clinically (Ardesch et al., 2010) (Table 2, Figure 1, Supplemental Figure 1 in Appendix 5). Our models reproduced threshold amplitudes required to activate laryngeal motor fibers across a range of pulse widths. Further, the activation thresholds across our nine modeled nerve morphologies captured the range of inter-individual variability (Figure 1(d)-(g), Supplemental Figure 1 in Appendix 5).

The stimulation amplitudes required to saturate the EMG signal were ~1 to 4x higher than the stimulation amplitudes that evoked EMG onset. As expected from inverse fiber recruitment order, the model thresholds for *larger* modeled fibers (i.e., lower activation thresholds) best reproduced the clinical EMG *onset* amplitudes and thresholds for *smaller* modeled fibers (i.e., higher activation thresholds) best reproduced the clinical EMG *saturation* amplitudes. More specifically, EMG onset amplitudes were best reproduced by 11.5 μm fibers (63.2 m/s), whereas EMG saturation amplitudes were best reproduced by 6.5 μm (31.3 m/s) fibers for longer pulse widths (>0.2 ms) and by 11.5 μm fibers (63.2 m/s) at shorter pulse widths (<0.2 ms) (Supplemental Figure 1 in Appendix 5). The latter effect, for EMG saturation amplitudes, follows from the observation that pulse widths >0.12 ms had little effect on clinical onset and saturation amplitudes, and only one clinical study evaluated shorter pulse widths, which yielded higher thresholds (Ardesch et al., 2010); thus, the modeled responses for the smaller, higher threshold fibers had a slightly longer chronaxie than the clinical EMG saturation data.

Aα fiber thresholds approximately doubled with the addition of encapsulation tissue (Figure 1(d),(e) versus (f),(g)), consistent with the acute versus chronic clinical EMG recordings (Bouckaert et al., 2022; Vespa et al., 2019). We uncoiled the helical LivaNova cuff as needed to accommodate the diameter of the nerve and encapsulation tissue, thereby increasing electrode-to-fiber distances and thereby also increasing the thresholds compared to our acute models.

The modeled B fiber thresholds were ~4 to 8x higher than the thresholds for the fastest Aα fibers, and ~2 to 3.5x higher than those of the slowest Aα fibers. For all fascicles in a modeled nerve, there was no overlap in threshold amplitudes for B fibers and the fastest Aα fibers, but there was overlap in 4/9 samples between thresholds for B fibers and the slowest Aα fibers.

Our modeled B fiber thresholds were consistent with clinical responses for short pulse widths (0.25 ms in (Premchand et al., 2014)), but underestimated thresholds at longer pulse widths (0.3–0.75 ms) (Figure 1(c), Appendix 6). We compared the heart rate responses to our model with encapsulation tissue because all published clinical data were recorded from patients with chronic implants.

The patient's heart rate in (Pascual, 2015) was <35 bpm with VNS turned on, indicating that the stimulation amplitude was well above threshold for B fibers at 0.5 ms pulse width;

indeed, the stimulation amplitude was above the modeled strength-duration data for B fiber onset across our population of human models (Figure 1(c)) and within the range of saturation thresholds (Appendix 6).

In (Premchand et al., 2014), 4/59 patients had modest bradycardia (i.e., HR reduction of 3–5 beats per minute), indicating that stimulation parameters for these individuals were close to bradycardia threshold at 0.25 ms pulse width; however the device parameters for the patients who experienced bradycardia acutely with VNS were not reported separately from the 55 patients who did not experience bradycardia. The mean stimulation amplitude delivered in the patient cohort was within the range of onset (Figure 1(c)) and below the range of saturation thresholds for our population of human models (Appendix 6), which is consistent with the observation that some but not all patients experienced bradycardia.

The patients in (Banzett et al., 1999) and (Zannad et al., 2015) did not exhibit VNS-evoked bradycardia. However, the stimulation amplitudes in (Banzett et al., 1999) were within the range of modeled onset to saturation thresholds, and the mean stimulation amplitude across 55 patients in (Zannad et al., 2015) was within the lower range of modeled thresholds (Figure 1(c), Appendix 6). Therefore, at pulse widths of 0.3 and 0.75 ms, our models underestimated B fiber thresholds, although factors not modeled herein may contribute to the cardiac responses to VNS.

Individual nerve morphology, encapsulation tissue, and fiber diameter had larger effects on model thresholds than correction for tissue shrinkage, the thickness of the saline layer, or the conductivities of the endoneurium or perineurium. In response to a 0.2 ms/phase biphasic pulse, thresholds of 11.5 μm diameter MRG fibers in acute human models varied by up to ~250% across samples (Figure 1(d)); encapsulation tissue increased thresholds ~100% across samples; across fiber diameters, thresholds increased ~100% and ~200% from 11.5 to 6.5 μm and 6.5 to 3 μm, respectively (Supplemental Figure 1(a), Figure 1(c)). Conversely, doubling or halving other parameters of the geometry and conductivity of the nerves resulted in <30% change in thresholds. Specifically, thresholds increased by ~20% for 11.5 μm diameter MRG fibers in a human vagus nerve (sample C57–3) when correcting for 20% shrinkage versus 10% shrinkage (Supplemental Figure 4 in Appendix 7). We halved or doubled the saline thickness between the cuff and the nerve (nominally 100 μm) for sample C57–3; thresholds for 11.5 μm diameter MRG fibers were ~20% lower and ~25% higher for 50 μm and 200 μm thicknesses, respectively (data not shown). Doubling or halving the nominal longitudinal endoneurium conductivity (i.e., 1/1.75 S/m) resulted in a ~30% increase and ~25% decrease in thresholds across modeled MRG fiber diameters, respectively; doubling or halving the nominal perineurium conductivity (i.e., 1/1149 S/m) resulted in a ~20% decrease and ~30% increase, respectively (Supplemental Figure 5 and Supplemental Figure 6 in Appendix 7). Thresholds for fibers in larger diameter fascicles were more sensitive to changes in material conductivities than thresholds for fibers in smaller diameter fascicles.

Pig VNS

We modeled histology from 8 pigs in which neural (CAP) and physiological (heart rate and laryngeal EMG) responses were recorded in vivo (Nicolai et al., 2020, 2021; Settell et al.,

2023). The range of model thresholds captured the in vivo responses for most EMG/Aα, all bradycardia/Aδ/B, and all Aγ response thresholds (Figure 2, black lines vs. black crosses). In vivo thresholds for EMG (2 animals) and Aα CAP responses (1 animal) were 0.1 mA, and the lowest model threshold for EMG/Aα (9.5 μm MRG) was 0.111 mA. The highest model threshold across fiber locations for some nerves was substantially higher than any in vivo threshold. Because we did not have information on functional topography, we modeled all fiber types in all fascicles, and therefore it is expected that the range of model thresholds will be wider than the in vivo range. Our models suggest that laryngeal fibers were in the fascicles that were closer to the electrode (i.e., surface of the epineurium), in smaller fascicles (which cause lower thresholds (Davis et al., 2023; Grinberg et al., 2008)), or both.

We also simulated thresholds using histology for the 12 pigs from (Pelot et al., 2020c, 2020b) (Figure 2, grey lines). Across fascicles (i.e., fiber locations), the lowest thresholds were comparable between both cohorts of pig nerves, but most (Nicolai et al., 2020, 2021; Settell et al., 2023) models included fiber locations with much higher thresholds. Therefore, the range of predicted thresholds for models based on histology from (Pelot et al., 2020c, 2020b) did not capture the highest in vivo thresholds. Onset and saturation thresholds for all fiber diameters in Table 2—which include the highest and lowest CV values used to ascribe CAP components to fiber types and the mean recorded CV—are shown in Supplemental Figure 7(a)-(e) in Appendix 8.

We also simulated fiber diameters using the animal-specific CV (Supplemental Table 2 in Appendix 8) reported for each component of the recorded CAP (Nicolai et al., 2020, 2021; Settell et al., 2023). For each pig, we plotted the threshold range for in vivo onset response, defined by the resolution of the amplitudes tested, versus the range of model thresholds across fiber locations. These boxes of response ranges spanned the 1:1 line (in vivo vs. model) for 6/8 Aα/Aβ (Figure 3(a)), 3/3 Aδ/B (Figure 3(b)), and 4/5 Aγ (Figure 3(c)) responses. The model threshold ranges (i.e., span between the lowest and highest threshold fascicles) were consistently larger than in vivo onset “ranges”. The former accounted for modeled thresholds for fibers in *all* fascicles (even though each in vivo response is only produced by a subset of fibers), while the latter accounted for amplitudes tested in vivo that first produced the CAP response and the next lowest amplitude. Our results suggest that medium and large myelinated fibers are in lower threshold fascicles (i.e., fascicles that are smaller and/or nearer to the nerve surface), or the models over-estimated thresholds. However, 3/5 Aγ responses (Figure 3(c)) show model saturation thresholds closer to in vivo onset thresholds, which either suggests Aγ fibers are in higher threshold fascicles in some individuals or the models underestimated thresholds in some instances.

For one model of pig VNS, we halved and doubled the saline thickness between the cuff and the nerve (nominally 100 μm) and found that thresholds for 9.5 μm diameter MRG fibers were ~25% lower and ~30% higher for 50 μm and 200 μm thicknesses, respectively.

Rat VNS

The thresholds for myelinated fibers in our model of rat VNS matched well the experimental thresholds from (Pelot & Grill, 2020) for “fast” fibers (>2 m/s, myelinated fiber model), especially for shorter pulse widths (<0.25 ms) (Figure 4(b)). At longer pulse widths,

the modeled thresholds did not capture some of the higher thresholds recorded in vivo. For modeled “slow” fiber diameters (<2 m/s, unmyelinated fiber model), the models overestimated the in vivo thresholds for most pulse widths (Figure 4(c)), but there was overlap for longer pulse widths (i.e., >0.3 ms).

We halved the saline thickness between the cuff and the nerve (nominally 10 μm); thresholds for 2.5 μm diameter MRG fibers were ~1% lower for the model with 5 μm thickness. The implementation of the Micro-Leads cuff in ASCENT did not allow the cuff to expand to accommodate increasing the saline thickness above 10 μm.

Discussion

Validated computational models, and publicly distributed software to implement them, are important and useful tools to advance peripheral nerve stimulation therapies. We demonstrated the robust built-in functionality of ASCENT to implement models of human, pig, and rat VNS, including a wide range of cuff electrode designs, stimulation parameters, nerve morphologies, and fiber types. Our work demonstrated the accuracy and limitations of the ASCENT models and highlighted the importance of modeling realistic nerve morphologies that are representative of the population.

Models Consistently Predict Thresholds for Myelinated Fibers

We used built-in features of ASCENT to model VNS in preclinical animals and humans and observed a strong quantitative match in nerve fiber activation thresholds. Our use of previously validated modeling methods, models, and biophysically realistic parameters produced robust agreement to corresponding in vivo data for threshold and saturation responses across a range of pulse widths and several fiber types. The match between experimental and modeled responses was consistent across an order of magnitude of nerve and cuff diameters, waveform pulse widths, and fiber diameters. Importantly, our process did not involve any tuning of model parameters to produce thresholds that matched experimental responses; all model parameters used published values and were not adjusted to match the published thresholds. In the process of validating human model responses against published clinical data, we learned that linking the models to appropriate in vivo data is critical for accurate comparisons. For example, we initially compared model Aα fiber thresholds to clinically tolerated stimulation amplitudes, an indirect measure of laryngeal EMG response, but direct measures of EMG dose-response curves were available in literature and were reproduced by our models.

Our models of human VNS matched well with the clinical thresholds for laryngeal EMG and are consistent with some reports of bradycardia; however, the clinical data used to validate our human model B fiber thresholds were reports of absence or presence of bradycardia rather than determination of individual thresholds. Consistent with fiber diameter recruitment order, where larger diameter fibers are activated at lower stimulation amplitudes than smaller diameter fibers, clinical EMG thresholds were reproduced by larger modeled Aα fibers, whereas the upper range of clinical EMG onset and saturation thresholds were captured by smaller modeled Aα fibers (Figure 1(d)-(g)). Our model B fiber thresholds were consistent with two reports of bradycardia in VNS patients (Pascual, 2015; Premchand

et al., 2014), and no patients experienced bradycardia at amplitudes less than modeled strength-duration data (Figure 1(c)). However, two different studies (Banzett et al., 1999; Zannad et al., 2015) suggest that our models underestimated B fiber thresholds for pulse widths >0.25 ms (Figure 1(c), Appendix 6) because patients with stimulation amplitudes higher than the modeled strength-duration data did not experience bradycardia. Based on the available data, there appear to be inconsistent reports of VNS parameters that induce bradycardia. In particular, since some of the patients in (Premchand et al., 2014) experienced bradycardia, we would expect that the patients programmed with longer pulse widths and higher amplitudes in (Banzett et al., 1999) would have also experienced a reduction in heart rate. In our acute and chronic human models, we observed saturation of fast Aα fibers before activation of any B fibers, but there was some overlap of B fiber recruitment with the slowest Aα fibers in about half of individuals. Lastly, the dynamic range of Aα fibers for pulse widths typically used in the clinic (i.e., 0.25 and 0.5 ms) is small relative to the amplitude step size of the LivaNova devices (i.e., 0.125 or 0.25 mA). Finer control of the output stimulation amplitude could enable better management of patient side effects and therapy.

The models of pig VNS captured the range of in vivo thresholds and choosing individualized fiber diameters based on recorded CV resulted in consistent agreement between modeled and experimental thresholds; however, pigs that had lower in vivo threshold ranges did not have lower corresponding model threshold ranges (Figure 3). Modeling all fiber types in all fascicles could explain the lack of threshold trend across individuals, and if the target fibers were in smaller fascicles and/or closer to the nerve surface, this distribution could also explain why the maximum model thresholds were consistently higher than in vivo thresholds specifically for Aα/Aβ and Aδ/B fibers (Figure 3). In contrast, Aγ fiber saturation thresholds (i.e., highest threshold fascicle) in 3/5 pig models agreed better with in vivo onset thresholds, thus suggesting that Aγ fibers are in higher threshold fascicles in some individuals or the models underestimated thresholds in some instances. Additionally, the model threshold ranges corresponding to the pig nerve morphologies in (Pelot et al., 2020b, 2020c) were consistently lower than the thresholds using the morphologies from (Nicolai et al., 2021). All (Nicolai et al., 2020) animals were implanted in vivo and modeled with the 2 mm LivaNova cuff regardless of nerve diameter, which resulted in larger electrode-fiber distances, and thus higher thresholds, for fascicles near the nerve boundary that was not in contact with the electrode. Further, the pigs in (Nicolai et al., 2021) had nerve diameters that were slightly larger (2.4–4.0 versus 2.3–3.4 mm in diameter, after correction for tissue shrinkage) (Supplemental Figure 7(f) in Appendix 8); the histology sections for the (Nicolai et al., 2020) pig nerves were taken closer to the nerve enlargement at the nodose ganglion (Settell et al., 2020).

Our models of human and pig VNS suggest that the pig is an appropriate preclinical animal model for development of VNS therapies. There is a large range of overlap between acute Aα fiber (~0.1–1.4 mA for pigs and ~0.1–0.5 mA for humans) and B fiber (~0.25–6 mA for pigs and ~0.5–5 mA for humans) thresholds for pig and human model populations with 0.2 ms pulse width. However, further physiological and mapping studies in pigs and humans are needed to confirm that equivalent nerve responses to stimulation produce common therapeutic and side-effects across species.

Our rat models reproduced experimental thresholds (Pelot & Grill, 2020) for “fast” fibers, especially for shorter pulse widths (Figure 4). Some in vivo thresholds were expected to be higher than model predictions because the slowest mammalian myelinated fiber that we modeled was 1 μm and had a CV of 7.65 m/s, which was slightly faster CV than the ~4–6 m/s CAP signal peaks in the “fast” experimental data from Figure 11 of (Pelot & Grill, 2020). Further work is needed to develop thinly myelinated fiber models with physiologically accurate CV; the smallest myelinated fibers in mammalian vagus nerves are ~1 μm (Guo et al., 1987; Licursi de Alcântara et al., 2008), but the CV for these model fibers is faster than the “fast” signals recorded in vivo.

More Accurate Vagal Unmyelinated Fiber Models Are Needed

Our models revealed differences in activation thresholds of unmyelinated C fibers compared to in vivo thresholds at short pulse widths. Although these fibers are unlikely to contribute to therapeutic mechanisms of VNS, as stimulation at the levels required to activate C fibers would be intolerable for patients (Chang et al., 2020; McAllen et al., 2018; Pelot & Grill, 2020; Yoo et al., 2013), this result highlights the need for improved biophysical cable models of unmyelinated C fibers. Especially at shorter pulse widths (<0.3 ms), the models overestimated in vivo thresholds for C fibers in rat. We used the Tigerholm C fiber model (Tigerholm et al., 2014), which better replicated experimental data than other published C fiber models (Pelot et al., 2021) and underwent robust parameterization and validation in the original publication. However, the Tigerholm C fiber model was not validated for responses to extracellular stimulation or developed specifically to represent vagal C fibers.

Populations of Models Reproduced Experimental Inter-Individual Variability

Our populations of models based on individual nerve morphologies from humans and pigs reproduced the inter-individual variability in thresholds observed in vivo. Most clearly, strength-duration data for models of human VNS narrowly bounded the range of laryngeal EMG thresholds (Figure 1(b)). In our models of human and pig VNS, nerve morphology and expansion of the LivaNova cuff to accommodate the nerve were the only model features that changed across individuals, resulting in inter-individual differences in activation thresholds. Nerve morphology varied widely across individuals, e.g., post-shrinkage correction nerve diameters for human and pig nerves ranged from 1.3–3.2 mm (2.5x) and 2.3–4.0 mm (1.7x), respectively. Even though the human nerves that we modeled are not those of the patients from whom the data were collected, our population of models reproduced the range of variability observed experimentally. However, incorporating the correct locations for each fiber type, which we assumed to be in all fascicles, would narrow the ranges of onset and saturation thresholds for neural and physiological responses in a population. Therefore, other sources of variability in VNS likely exist, such as differences in development of encapsulation tissue at the implant or changes from plasticity or neural accommodation.

According to our models, differences in nerve morphology within a population result in variability in the stimulation amplitudes required to achieve a targeted nerve response in an individual. The stimulation parameters used in clinical studies for epilepsy (chronic: 1.3 mA, 0.5 ms) (Handforth et al., 1998), heart failure (chronic: 1.7 ± 0.5 mA, 0.25 ms) (Premchand et al., 2014), and rheumatoid arthritis (acute: 1 mA, 0.5 ms) (Koopman et al.,

2016) saturated fast Aα fibers and activated at least some slow Aα fibers in all human models (Figure 1, Appendix 5). For the stimulation parameters used across these studies, onset of B fiber activation occurred in some but not all models, and B fibers were not saturated in any models. For the stimulation parameters used in the epilepsy patients in (Handforth et al., 1998), our models predict slow Aα fiber saturation and B fiber onset in 9/9 and 4/9 nerves, respectively. For the stimulation parameters used in the heart failure patients in (Premchand et al., 2014), our models predict slow Aα fiber saturation and B fiber onset in in 5/9 and 3/9 nerves, respectively. Lastly, for the stimulation parameters used in the rheumatoid arthritis patients in (Koopman et al., 2016), our models predict slow Aα fiber saturation and B fiber onset in 3/9 nerves. The stimulation parameters used in clinical studies for stroke (chronic: 0.8 mA, 0.2 ms) (Dawson et al., 2021; Kimberley et al., 2018) produced fast Aα fiber onset in all (Figure 1(f)), fast Aα saturation in 4/9 (Figure 1(g)), and slow Aα fiber onset in 3/9 human models (Supplemental Figure 1(c) in Appendix 5); the models do not predict slow Aα fiber saturation (Supplemental Figure 1(d) in Appendix 5) or B fiber onset (Figure 1(c)) in any human nerves. Our models demonstrate that to target nerve responses in an individual, specific morphology must be considered to identify where the nerve's response falls within the population's distribution of responses to a given stimulus.

Encapsulation Tissue Increased Model Thresholds

Incorporating encapsulation tissue in the models increased activation thresholds by ~70–130% (Figure 1(d),(e) versus (f),(g)). Previous modeling work showed conflicting effect sizes of nerve encapsulation tissue on fiber thresholds. Specifically, one modeling study of subdiaphragmatic VNS found that removing encapsulation tissue had minimal effect on activation and block thresholds (i.e., block thresholds were ~3–8 mA with encapsulation tissue and decreased <1 mA without encapsulation) (Pelot et al., 2017), but another study modeling splenic nerve stimulation found thresholds increased ~50% by adding encapsulation tissue (Gupta et al., 2020). (Gupta et al., 2020) used a 500 μm thick encapsulation tissue layer based on (Grill & Mortimer, 1994), and (Pelot et al., 2017) used a 150 μm thick layer based on (Haberler et al., 2000; Moss et al., 2004). We increased the encapsulation tissue layer thickness from 150 μm used in (Pelot et al., 2017) to 250 μm, which is an approximately halfway between the ~450 μm thickness reported in (Grill & Mortimer, 1994) and the sources used by (Pelot et al., 2017). Additionally, our study included a 100 μm thick saline layer between the cuff and the encapsulation tissue, which was informed by video from a VNS explant surgery (Aalbers et al., 2015). The saline layer in our models, which is more conductive than encapsulation tissue, shunted current between the contacts, thereby increasing thresholds.

The increase in thresholds from acute to chronic implants could also be attributed to factors which we did not model. Specifically, our models do not account for habituation (Dutschmann et al., 2014; Siniaia et al., 2000) or synaptic plasticity (Hays et al., 2013). Although our models demonstrate that encapsulation tissue likely plays a role in the increase of thresholds from acute to chronic settings, in vivo studies are required to assess the contributions of alternative mechanisms. Further, by identifying the nerve fibers that are activated with specific parameters, these results constrain the potential mechanisms underlying different therapies.

Discrepancy Between Aα Fiber Thresholds and Clinically Tolerated Amplitudes

VNS amplitudes used in patients are limited by laryngeal muscle activation (hoarseness, throat pain, coughing) at higher amplitudes (The Vagus Nerve Stimulation Study Group, 1995). Aα fiber thresholds in our models of human VNS were consistent with clinical thresholds for laryngeal EMG onset (i.e., ~0.25–0.5 mA) (Ardesch et al., 2010; Bouckaert et al., 2022; Vespa et al., 2019) and saturation (i.e., ~0.5–1 mA) (Bouckaert et al., 2022; Vespa et al., 2019), but model and laryngeal EMG saturation thresholds were lower than clinically tolerated stimulation amplitudes (e.g., 2.1 mA) (Premchand et al., 2014). Indeed, all clinical VNS studies report high rates of side-effects related to laryngeal muscle activation such as hoarseness or coughing. Therefore, our models suggest that for most patients, the therapy-limiting side-effects are either driven by responses of fibers which we did not model, such as those in nearby branches from current leakage outside the cuff (Nicolai et al., 2020), or patient tolerance to side-effects increases due to changes in neural and physiological pathways over time (Uthman et al., 1993).

Although yet to be confirmed in humans, our models support a previously published claim that noxious sensations likely result from activation of nearby branches due to current leakage in addition to activation of fibers inside the cuff (Nicolai et al., 2020). Our source of pig electrophysiology and histology data (Nicolai et al., 2020) identified long- and short-latency EMG components that arose distinctly from activation of fibers in the main trunk via the recurrent laryngeal branches and in branches that course near but outside of the cuff (i.e., the superior laryngeal branch), respectively. As expected, we found that our modeled pig VNS thresholds agreed well with the lower thresholds for the fibers in the main trunk and the associated long-latency EMG component; in vivo thresholds for activating the superior laryngeal branch were higher than the saturation threshold for modeled fibers in the main trunk. Therefore, our results suggest that cuff designs that reduce current leakage will increase the range of fiber types that can be activated in the nerve trunk without producing intolerable concomitant side effects related to current leakage and activation of nearby branches.

Chronic nerve stimulation could result in changes to neural and physiological pathways that may explain why patients tolerate higher VNS amplitudes over time (Uthman et al., 1993). Synaptic plasticity in the brain could affect how the central nervous system processes sensory signals from laryngeal muscle activation (Hays et al., 2013). With increased activity, morphological changes could occur at the synapse of motor fibers onto the laryngeal muscles and affect how signals are transmitted at the neuromuscular junction (Deschenes et al., 2006). Further, the laryngeal muscles could adapt to increased activation in a variety of ways (Salmons & Henriksson, 1981), which could affect the tolerability of VNS.

Limitations

Incorporating additional information from the experiments into our models could yield improved accuracy. Specifically, our models would benefit from more precise correction for tissue shrinkage, measurements of saline layer thickness between the cuff and surrounding tissues, detailed mapping of nerve microanatomy, modeling the passive recharge phase used clinically in the LivaNova device, and higher resolution of amplitudes tested in vivo. Further,

certain physiological responses that we used to validate our models are more complex than our in silico representation of direct neural stimulation (e.g., afferent/efferent effects, sympathetic responses, reflex responses, plasticity in response to chronic stimulation).

Our models may overcorrect for the tissue shrinkage that occurs from dehydration and heating during histological processing. We showed that overcorrecting for shrinkage results in overestimation of thresholds due to increased fascicle diameter, perineurium thickness, and electrode-fiber distance. Shrinkage amounts vary with different histology methods, and we extrapolated estimates for bulk tissue shrinkage from data of individual fiber shrinkage which may be inaccurate; peripheral nerve myelinated fibers have been shown to shrink ~20–30% (Boyd & Kalu, 1979; Friede & Samorajski, 1967). Further analyses to quantify tissue shrinkage during histology or alternative imaging modalities to determine in vivo nerve diameters should be considered.

Information about the thickness of fluid between the cuff and the nerve could improve the accuracy of the thresholds predicted by our models. In particular, the human and pig model thresholds were sensitive to halving (i.e., ~20–25% lower) or doubling (~25–30% higher) the thickness of the layer from our 100 μm thick layer. In contrast, our rat model thresholds were virtually unaffected by halving the thickness of the saline layer (i.e., ~1%) from our 10 μm thick layer, likely due to the small 5 μm change in saline thickness, versus the 50 μm change in the pig and human models.

Further, we assumed that all fiber diameters and types were placed in all fascicles, thus neglecting spatial organization of fiber types in the nerve cross section. Recent studies show organ-specific fascicular organization in pigs and humans (Jayaprakash et al., 2022; Thompson et al., 2022), and that fascicles split, merge, and re-join (Upadhye et al., 2022). In the histology that we used to develop our models, we do not know which fascicles contained the fibers that produced the CAP or physiological responses used for validation, and we know that CAP recordings will not capture the response for all fibers with the same sensitivity; therefore, in comparing threshold and saturation, we considered the range of thresholds across all model fascicles. Previous work studying spatially-selective VNS in pigs incorporated nerve vagotopy (Blanz et al., 2023), but this information was not available for the nerves modeled here. Inclusion of vagotopy qualitatively shifted experimental dose-response curves toward improved match in most animals, but the study lacked sufficient sample size, in vivo threshold resolution, and model detail (e.g., specific fascicles for laryngeal EMG or cardiac responses) to achieve statistical significance. Additionally, we simulated fibers at discrete diameters rather than for a distribution of diameters. For optimal quantitative match in an individual, particularly at intermediate response levels, models may require specific diameters for each fiber in the nerve. By modeling all fiber diameters in all fascicles, our methods for defining threshold and saturation captured more realistically the range of in vivo thresholds across a population.

The LivaNova implanted pulse generator has a passive recharge secondary phase that we approximated to be rectangular. The charge delivered across the electrodes from the primary phase discharges passively during the secondary phase (LivaNova R&D, personal communication, April 12, 2021). Since the peak current amplitude and shape of the

secondary phase are not publicly available, we compared thresholds in response to biphasic symmetric pulses, as used throughout the models herein, to thresholds in response to monophasic pulses for pulse widths of 0.05–1 ms. With a monophasic pulse, thresholds for 11.5 μm MRG fibers decreased by ~20% for the shortest pulse widths. However, for the longest pulse widths, thresholds increased by ~5%.

We are limited by the resolution of the amplitudes tested in vivo and clinically, which defines the range between which fibers reached activation threshold or saturation. The number of stimulation parameter combinations tested is critically limited by maximum surgery or office visit duration and the time required to test each parameter combination.

The in vivo and clinical heart rate data that we used to validate our B fiber thresholds in humans and pigs is a suboptimal substitute for direct quantification of B fiber response. Specifically, thresholds for bradycardia are not reported explicitly in the literature, saturation thresholds are not feasible due to safety considerations, and the best sources to validate our models often report summary statistics for the entire cohort of patients (i.e., patients with and without bradycardia) thereby obfuscating individual patient responses.

Lastly, the finite element models created by ASCENT assumed quasi-static conditions for approximating electric fields (Bossetti et al., 2007) and omitted the impedance of the electrode-electrolyte interface (Cantrell et al., 2007; Newman, 1966), but neither of these assumptions limit our accuracy in predicting nerve responses to low frequency current-controlled stimulation. Further, our models do not incorporate known variations in nerve cross section that occur along its length (Upadhye et al., 2022); true three-dimensional nerve morphology would alter the electrode-fiber distances and could have pronounced effects on threshold of specific fibers, particularly for cuffs with large contact pitch.

Conclusions

ASCENT allowed faithful implementation of nerve morphology and cuff geometry across a wide range of experimental configurations. The specific ASCENT models produced accurate fiber activation thresholds for VNS across a range of species, fiber types, and waveforms. Validated computational models are important tools for analysis and design of peripheral nerve interfaces for stimulation and recording.

Supplementary Material

Refer to Web version on PubMed Central for supplementary material.

Acknowledgments

Funding for this work was provided by the NIH SPARC Program (OT2 OD025340). Thanks to Daniel Marshall for helping to segment pig nerve histology to serve as inputs to ASCENT. Thanks to Megan Settell for sharing nerve histology to make models of the experiments in (Nicolai et al., 2020). Thanks to Minhaj Hussain for preliminary work on modeling rat VNS.

Data Availability

All data are available at the following DOI: https://doi.org/10.26275/vdpw-rjqu

References

Aalbers MW, Rijkers K, Klinkenberg S, Majoie M, & Cornips EMJ (2015). Vagus nerve stimulation lead removal or replacement: surgical technique, institutional experience, and literature overview. Acta Neurochirurgica, 157(11), 1917–1924. 10.1007/s00701-015-2547-9 [PubMed: 26335753]

Ardesch JJ, Sikken JR, Veltink PH, van der Aa HE, Hageman G, & Buschman HPJ (2010). Vagus nerve stimulation for epilepsy activates the vocal folds maximally at therapeutic levels. Epilepsy Research, 89(2), 227–231. 10.1016/j.eplepsyres.2010.01.005 [PubMed: 20129758]

Aristovich K, Donega M, Fjordbakk C, Tarotin I, Chapman CAR, Viscasillas J, Stathopoulou T-R, Crawford A, Chew D, Perkins J, & Holder D (2021). Model-based geometrical optimisation and in vivo validation of a spatially selective multielectrode cuff array for vagus nerve neuromodulation. Journal of Neuroscience Methods, 352, 109079. 10.1016/j.jneumeth.2021.109079 [PubMed: 33516735]

Arle JE, Carlson KW, & Mei L (2016). Investigation of mechanisms of vagus nerve stimulation for seizure using finite element modeling. Epilepsy Research, 126, 109–118. 10.1016/j.eplepsyres.2016.07.009 [PubMed: 27484491]

Banzett RB, Guz A, Paydarfar D, Shea SA, Schachter SC, & Lansing RW (1999). Cardiorespiratory variables and sensation during stimulation of the left vagus in patients with epilepsy. Epilepsy Research, 35(1), 1–11. 10.1016/S0920-1211(98)00126-0 [PubMed: 10232789]

Blanz SL, Musselman ED, Settell ML, Knudsen BE, Nicolai EN, Trevathan JK, Verner RS, Begnaud J, Skubal AC, Suminski AJ, Williams JC, Shoffstall AJ, Grill WM, Pelot NA, & Ludwig KA (2023). Spatially selective stimulation of the pig vagus nerve to modulate target effect versus side effect. Journal of Neural Engineering. 10.1088/1741-2552/acb3fd

Bossetti CA, Birdno MJ, & Grill WM (2007). Analysis of the quasi-static approximation for calculating potentials generated by neural stimulation. Journal of Neural Engineering, 5(1), 44–53. 10.1088/1741-2560/5/1/005 [PubMed: 18310810]

Bouckaert C, Raedt R, Larsen LE, El Tahry R, Gadeyne S, Carrette E, Proesmans S, Dewaele F, Delbeke J, De Herdt V, Meurs A, Mertens A, Boon P, & Vonck K (2022). Laryngeal Muscle-Evoked Potential Recording as an Indicator of Vagal Nerve Fiber Activation. Neuromodulation: Technology at the Neural Interface, 25(3), 461–470. 10.1016/j.neurom.2022.01.014 [PubMed: 35177376]

Boyd IA, & Kalu KU (1979). Scaling factor relating conduction velocity and diameter for myelinated afferent nerve fibres in the cat hind limb. The Journal of Physiology, 289, 277–297. 10.1113/jphysiol.1979.sp012737 [PubMed: 458657]

Bucksot JE, Chandler CR, Intharuck NM, Rennaker RL, Kilgard MP, & Hays SA (2021). Validation of a parameterized, open-source model of nerve stimulation. Journal of Neural Engineering, 18(4), 42001. 10.1088/1741-2552/ac1983

Callister WD, & Rethwisch DG (2012). Fundamentals of Material Science and Engineering An Integrated Approach. In Fundamentals Of Material Science and Engineering An Intergrated Approach.

Cantrell DR, Inayat S, Taflove A, Ruoff RS, & Troy JB (2007). Incorporation of the electrode--electrolyte interface into finite-element models of metal microelectrodes. Journal of Neural Engineering, 5(1), 54–67. 10.1088/1741-2560/5/1/006 [PubMed: 18310811]

Chang Y-C, Cracchiolo M, Ahmed U, Mughrabi I, Gabalski A, Daytz A, Rieth L, Becker L, Datta-Chaudhuri T, Al-Abed Y, Zanos TP, & Zanos S (2020). Quantitative estimation of nerve fiber engagement by vagus nerve stimulation using physiological markers. Brain Stimulation, 13(6), 1617–1630. 10.1016/j.brs.2020.09.002 [PubMed: 32956868]

Dali M, Rossel O, Andreu D, Laporte L, Hernández A, Laforet J, Marijon E, Hagège A, Clerc M, Henry C, & Guiraud D (2018). Model based optimal multipolar stimulation without *a priori* knowledge of nerve structure: application to vagus nerve stimulation. Journal of Neural Engineering, 15(4), 46018. 10.1088/1741-2552/aabeb9

Davis CJ, Musselman ED, Grill WM, & Pelot NA (2023). Fibers in smaller fascicles have lower activation thresholds with cuff electrodes due to thinner perineurium and smaller cross-sectional area. Journal of Neural Engineering 10.1088/1741-2552/acc42b

Dawson J, Liu CY, Francisco GE, Cramer SC, Wolf SL, Dixit A, Alexander J, Ali R, Brown BL, Feng W, DeMark L, Hochberg LR, Kautz SA, Majid A, O'Dell MW, Pierce D, Prudente CN, Redgrave J, Turner DL, … Kimberley TJ (2021). Vagus nerve stimulation paired with rehabilitation for upper limb motor function after ischaemic stroke (VNS-REHAB): a randomised, blinded, pivotal, device trial. Lancet (London, England), 397(10284), 1545–1553. 10.1016/S0140-6736(21)00475-X [PubMed: 33894832]

de Podesta M, Laboratory NP, & UK. (1996). Understanding the Properties of Matter. In Understanding the Properties of Matter. 10.4324/9780203450611

Deschenes MR, Tenny KA, & Wilson MH (2006). Increased and decreased activity elicits specific morphological adaptations of the neuromuscular junction. Neuroscience, 137(4), 1277–1283. 10.1016/j.neuroscience.2005.10.042 [PubMed: 16359818]

Deurloo KE, Holsheimer J, & Boom HB (1998). Transverse tripolar stimulation of peripheral nerve: a modelling study of spatial selectivity. Medical & Biological Engineering & Computing, 36(1), 66–74. 10.1007/BF02522860 [PubMed: 9614751]

Deurloo KEI, Holsheimer J, & Bergveld P (2000). Nerve Stimulation With A Multi-Contact Cuff Electrode: Validation Of Model Predictions. Archives of Physiology and Biochemistry, 108(4), 349–359. 10.1076/apab.108.4.349.4301 [PubMed: 11094386]

Dutschmann M, Bautista TG, Mörschel M, & Dick TE (2014). Learning to breathe: habituation of Hering-Breuer inflation reflex emerges with postnatal brainstem maturation. Respiratory Physiology & Neurobiology, 195, 44–49. 10.1016/j.resp.2014.02.009 [PubMed: 24566392]

Eiber CD, Payne SC, Biscola NP, Havton LA, Keast JR, Osborne PB, & Fallon JB (2021). Computational modelling of nerve stimulation and recording with peripheral visceral neural interfaces. Journal of Neural Engineering, 18(6). 10.1088/1741-2552/ac36e2

Fang Z-P, & Mortimer JT (1991). Selective activation of small motor axons by quasitrapezoidal current pulses. IEEE Transactions on Biomedical Engineering, 38(2), 168–174. 10.1109/10.76383 [PubMed: 2066126]

Friede RL, & Samorajski T (1967). Relation between the number of myelin lamellae and axon circumference in fibers of vagus and sciatic nerves of mice. The Journal of Comparative Neurology, 130(3), 223–231. 10.1002/cne.901300304 [PubMed: 6036111]

Frieswijk TA, Smit JPA, Rutten WLC, & Boom HBK (1998). Force-current relationships in intraneural stimulation: role of extraneural medium and motor fibre clustering. Medical and Biological Engineering and Computing, 36(4), 422–430. 10.1007/BF02523209 [PubMed: 10198524]

Gielen FLH, Wallinga-de Jonge W, & Boon KL (1984). Electrical conductivity of skeletal muscle tissue: Experimental results from different musclesin vivo. Medical and Biological Engineering and Computing, 22(6), 569–577. 10.1007/BF02443872 [PubMed: 6503387]

Grill WM, & Mortimer TJ (1994). Electrical properties of implant encapsulation tissue. Annals of Biomedical Engineering, 22(1), 23–33. 10.1007/BF02368219 [PubMed: 8060024]

Grinberg Y, Schiefer MA, Tyler DJ, & Gustafson KJ (2008). Fascicular perineurium thickness, size, and position affect model predictions of neural excitation. IEEE Transactions on Neural Systems and Rehabilitation Engineering : A Publication of the IEEE Engineering in Medicine and Biology Society, 16(6), 572–581. 10.1109/TNSRE.2008.2010348 [PubMed: 19144589]

Guo YP, McLeod JG, & Baverstock J (1987). Pathological changes in the vagus nerve in diabetes and chronic alcoholism. Journal of Neurology, Neurosurgery, and Psychiatry, 50(11), 1449–1453. 10.1136/jnnp.50.11.1449 [PubMed: 3694205]

Gupta I, Cassará AM, Tarotin I, Donega M, Miranda JA, Sokal DM, Ouchouche S, Dopson W, Matteucci P, Neufeld E, Schiefer MA, Rowles A, McGill P, Perkins J, Dolezalova N, Saeb-Parsy K, Kuster N, Yazicioglu RF, Witherington J, & Chew DJ (2020). Quantification of clinically applicable stimulation parameters for precision near-organ neuromodulation of human splenic nerves. Communications Biology, 3(1), 577. 10.1038/s42003-020-01299-0 [PubMed: 33067560]

Haberler C, Alesch F, Mazal PR, Pilz P, Jellinger K, Pinter MM, Hainfellner JA, & Budka H (2000). No tissue damage by chronic deep brain stimulation in Parkinson's disease. Annals of Neurology, 48(3), 372–376. [PubMed: 10976644]

Handforth A, DeGiorgio CM, Schachter SC, Uthman BM, Naritoku DK, Tecoma ES, Henry TR, Collins SD, Vaughn BV, Gilmartin RC, Labar DR, Morris GL 3rd, Salinsky MC, Osorio I,

Ristanovic RK, Labiner DM, Jones JC, Murphy JV, Ney GC, & Wheless JW (1998). Vagus nerve stimulation therapy for partial-onset seizures: a randomized active-control trial. Neurology, 51(1), 48–55. 10.1212/wnl.51.1.48 [PubMed: 9674777]

Hays SA, Rennaker RL, & Kilgard MP (2013). Targeting plasticity with vagus nerve stimulation to treat neurological disease. Progress in Brain Research, 207, 275–299. 10.1016/B978-0-444-63327-9.00010-2 [PubMed: 24309259]

Helmers SL, Begnaud J, Cowley A, Corwin HM, Edwards JC, Holder DL, Kostov H, Larsson PG, Levisohn PM, De Menezes MS, Stefan H, & Labiner DM (2012). Application of a computational model of vagus nerve stimulation. Acta Neurologica Scandinavica, 126(5), 336–343. 10.1111/j.1600-0404.2012.01656.x [PubMed: 22360378]

Hines ML, & Carnevale NT (1997). The NEURON simulation environment. Neural Computation, 9(6), 1179–1209. 10.1162/neco.1997.9.6.1179 [PubMed: 9248061]

Horch K (2017). Neuroprosthetics: Theory and practice: Second edition. In Neuroprosthetics: Theory and Practice: Second Edition. 10.1142/10368

Howell B, & Grill WM (2014). Evaluation of high-perimeter electrode designs for deep brain stimulation. Journal of Neural Engineering, 11(4), 46026. 10.1088/1741-2560/11/4/046026

Howell B, Naik S, & Grill WM (2014). Influences of Interpolation Error, Electrode Geometry, and the Electrode–Tissue Interface on Models of Electric Fields Produced by Deep Brain Stimulation. IEEE Transactions on Biomedical Engineering, 61(2), 297–307. 10.1109/TBME.2013.2292025 [PubMed: 24448594]

Hursh JB (1939). CONDUCTION VELOCITY AND DIAMETER OF NERVE FIBERS. American Journal of Physiology-Legacy Content, 127(1), 131–139. 10.1152/ajplegacy.1939.127.1.131

Jayaprakash N, Song W, Toth V, Vardhan A, Levy T, Tomaio J, Qanud K, Mughrabi I, Chang Y-C, Rob M, Daytz A, Abbas A, Nassrallah Z, Volpe BT, Tracey KJ, Al-Abed Y, Datta-Chaudhuri T, Miller L, Barbe MF, … Zanos S (2022). Organ- and function-specific anatomical organization of the vagus nerve supports fascicular vagus nerve stimulation. BioRxiv, 2022.03.07.483266. 10.1101/2022.03.07.483266

Katz B, & Miledi R (1965). The effect of temperature on the synaptic delay at the neuromuscular junction. The Journal of Physiology, 181(3), 656–670. 10.1113/jphysiol.1965.sp007790 [PubMed: 5880384]

Kimberley TJ, Pierce D, Prudente CN, Francisco GE, Yozbatiran N, Smith P, Tarver B, Engineer ND, Alexander Dickie D, Kline DK, Wigginton JG, Cramer SC, & Dawson J (2018). Vagus Nerve Stimulation Paired With Upper Limb Rehabilitation After Chronic Stroke. Stroke, 49(11), 2789–2792. 10.1161/STROKEAHA.118.022279 [PubMed: 30355189]

Koopman FA, Chavan SS, Miljko S, Grazio S, Sokolovic S, Schuurman PR, Mehta AD, Levine YA, Faltys M, Zitnik R, Tracey KJ, & Tak PP (2016). Vagus nerve stimulation inhibits cytokine production and attenuates disease severity in rheumatoid arthritis. Proceedings of the National Academy of Sciences of the United States of America, 113(29), 8284–8289. 10.1073/pnas.1605635113 [PubMed: 27382171]

Kotby MN, Fadly E, Madkour O, Barakah M, Khidr A, Alloush T, & Saleh M (1992). Electromyography and neurography in neurolaryngology. Journal of Voice, 6(2), 159–187. 10.1016/S0892-1997(05)80131-6

Krahl SE (2012). Vagus nerve stimulation for epilepsy: A review of the peripheral mechanisms. Surgical Neurology International, 3(Suppl 1), S47–52. 10.4103/2152-7806.91610 [PubMed: 22826811]

Lazorchak N, Horn MR, Muzquiz MI, Mintch LM, & Yoshida K (2022). Accurate simulation of cuff electrode stimulation predicting in-vivo strength-duration thresholds. Artificial Organs, n/a(n/a). 10.1111/aor.14374

Licursi de Alcântara AC, Salgado HC, & Sassoli Fazan VP (2008). Morphology and morphometry of the vagus nerve in male and female spontaneously hypertensive rats. Brain Research, 1197, 170–180. 10.1016/j.brainres.2007.12.045 [PubMed: 18234157]

McAllen RM, Shafton AD, Bratton BO, Trevaks D, & Furness JB (2018). Calibration of thresholds for functional engagement of vagal A, B and C fiber groups in vivo. Bioelectronics in Medicine, 1(1), 21–27. 10.2217/bem-2017-0001 [PubMed: 29480903]

McIntyre CC, Grill WM, Sherman DL, & Thakor NV (2004). Cellular effects of deep brain stimulation: model-based analysis of activation and inhibition. Journal of Neurophysiology, 91(4), 1457–1469. 10.1152/jn.00989.2003 [PubMed: 14668299]

McIntyre CC, Richardson AG, & Grill WM (2002). Modeling the excitability of mammalian nerve fibers: influence of afterpotentials on the recovery cycle. Journal of Neurophysiology, 87(2), 995–1006. 10.1152/jn.00353.2001 [PubMed: 11826063]

Moss J, Ryder T, Aziz TZ, Graeber MB, & Bain PG (2004). Electron microscopy of tissue adherent to explanted electrodes in dystonia and Parkinson's disease. Brain : A Journal of Neurology, 127(Pt 12), 2755–2763. 10.1093/brain/awh292 [PubMed: 15329356]

Musselman ED, Cariello JE, Grill WM, & Pelot NA (2021). ASCENT (Automated Simulations to Characterize Electrical Nerve Thresholds): A Pipeline for Sample-Specific Computational Modeling of Electrical Stimulation of Peripheral Nerves. PLoS Computational Biology 10.1371/journal.pcbi.1009285

Musselman ED, Pelot NA, & Grill WM (2023). Validated Computational Models Predict Vagus Nerve Stimulation Thresholds in Preclinical Animals and Humans (Version 1) [Dataset]. SPARC Consortium. 10.26275/vdpw-rjqu

Newman J (1966). Current Distribution on a Rotating Disk below the Limiting Current. J. Electrochem. Soc, 113, 1235–1241.

Nicolai EN, Settell ML, Knudsen BE, McConico AL, Gosink BA, Trevathan JK, Baumgart IW, Ross EK, Pelot NA, Grill WM, Gustafson KJ, Shoffstall AJ, Williams JC, & Ludwig KA (2020). Sources of Off-Target Effects of Vagus Nerve Stimulation Using the Helical Clinical Lead in Domestic Pigs. Journal of Neural Engineering, 17(4), 046017. 10.1088/1741-2552/ab9db8 [PubMed: 32554888]

Nicolai EN, Settell ML, Knudsen BE, McConico AL, Gosink BA, Trevathan JK, Baumgart IW, Ross EK, Pelot NA, Grill WM, Gustafson KJ, Shoffstall AJ, Williams JC, & Ludwig KA (2021). Sources of off-target effects for vagus nerve stimulation using the LivaNova clinical lead in swine (Version 1) [Data set]. SPARC Consortium. 10.26275/QCUK-A8TY

Pascual FT (2015). Vagus nerve stimulation and late-onset bradycardia and asystole: Case report. Seizure - European Journal of Epilepsy, 26, 5–6. 10.1016/j.seizure.2015.01.006 [PubMed: 25799894]

Pelot NA, Behrend CE, & Grill WM (2017). Modeling the response of small myelinated axons in a compound nerve to kilohertz frequency signals. Journal of Neural Engineering, 14(4), 46022. 10.1088/1741-2552/aa6a5f

Pelot NA, Behrend CE, & Grill WM (2019). On the parameters used in finite element modeling of compound peripheral nerves. Journal of Neural Engineering, 16(1), 16007. 10.1088/1741-2552/aaeb0c

Pelot NA, Catherall DC, Thio BJ, Titus ND, Liang ED, Henriquez CS, & Grill WM (2021). Excitation properties of computational models of unmyelinated peripheral axons. Journal of Neurophysiology, 125(1), 86–104. 10.1152/jn.00315.2020 [PubMed: 33085556]

Pelot NA, Ezzell JA, Goldhagen GB, Cariello JE, Clissold KA, & Grill WM (2020a). Quantified morphology of the human vagus nerve with anti-claudin-1 (Version 6) [Data set]. SPARC Consortium. 10.26275/OFJA-GHOZ

Pelot NA, Goldhagen GB, Cariello JE, & Grill WM (2020b). Quantified morphology of the pig vagus nerve (Version 4) [Data set]. SPARC Consortium. 10.26275/MAQ2-EII4

Pelot NA, Goldhagen GB, Cariello JE, Musselman ED, Clissold KA, Ezzell JA, & Grill WM (2020c). Quantified Morphology of the Cervical and Subdiaphragmatic Vagus Nerves of Human, Pig, and Rat. Frontiers in Neuroscience, 14, 1148. 10.3389/fnins.2020.601479

Pelot NA, & Grill WM (2020). In vivo quantification of excitation and kilohertz frequency block of the rat vagus nerve. Journal of Neural Engineering, 17(2), 26005. 10.1088/1741-2552/ab6cb6

Pelot NA, Thio BJ, & Grill WM (2018). Modeling Current Sources for Neural Stimulation in COMSOL. Frontiers in Computational Neuroscience, 12, 40. 10.3389/fncom.2018.00040 [PubMed: 29937722]

Prades JM, Dubois MD, Dumollard JM, Tordella L, Rigail J, Timoshenko AP, & Peoc'h M (2012). Morphological and functional asymmetry of the human recurrent laryngeal nerve. Surgical and Radiologic Anatomy : SRA, 34(10), 903–908. 10.1007/s00276-012-0999-7 [PubMed: 23150169]

Premchand RK, Sharma K, Mittal S, Monteiro R, Dixit S, Libbus I, DiCarlo LA, Ardell JL, Rector TS, Amurthur B, KenKnight BH, & Anand IS (2014). Autonomic regulation therapy via left or right cervical vagus nerve stimulation in patients with chronic heart failure: results of the ANTHEM-HF trial. Journal of Cardiac Failure, 20(11), 808–816. 10.1016/j.cardfail.2014.08.009 [PubMed: 25187002]

Ranck JB, & BeMent SL (1965). The specific impedance of the dorsal columns of cat: An anisotropic medium. Experimental Neurology, 11(4), 451–463. 10.1016/0014-4886(65)90059-2 [PubMed: 14278100]

Raspopovic S, Capogrosso M, Badia J, Navarro X, & Micera S (2012). Experimental Validation of a Hybrid Computational Model for Selective Stimulation Using Transverse Intrafascicular Multichannel Electrodes. IEEE Transactions on Neural Systems and Rehabilitation Engineering, 20(3), 395–404. 10.1109/TNSRE.2012.2189021 [PubMed: 22481834]

Rohatgi A (2022). Webplotdigitizer: Version 4.6. https://automeris.io/WebPlotDigitizer

Romero E, Denef JF, Delbeke J, Robert A, & Veraart C (2001). Neural morphological effects of long-term implantation of the self-sizing spiral cuff nerve electrode. Medical and Biological Engineering and Computing, 39(1), 90–100. 10.1007/BF02345271 [PubMed: 11214279]

Salmons S, & Henriksson J (1981). The adaptive response of skeletal muscle to increased use. Muscle & Nerve, 4(2), 94–105. 10.1002/mus.880040204 [PubMed: 7010156]

Schnitzlein HN, Rowe LC, & Hoffman HH (1958). The myelinated component of the vagus nerves in man. The Anatomical Record, 131(4), 649–667. 10.1002/ar.1091310404

Settell ML, Ludwig KA, Knudsen BE, Pelot NA, & Nicolai EN (2023). Histology of pig cervical vagus nerve (Version 1) [Data set]. SPARC Consortium. 10.26275/F5SE-YNPK

Settell ML, Pelot NA, Knudsen BE, Dingle AM, McConico AL, Nicolai EN, Trevathan JK, Ezzell JA, Ross EK, Gustafson KJ, Shoffstall AJ, Williams JC, Zeng W, Poore SO, Populin LC, Suminski AJ, Grill WM, & Ludwig KA (2020). Functional vagotopy in the cervical vagus nerve of the domestic pig: implications for the study of vagus nerve stimulation. Journal of Neural Engineering, 17(2), 26022. 10.1088/1741-2552/ab7ad4

Siniaia MS, Young DL, & Poon CS (2000). Habituation and desensitization of the Hering-Breuer reflex in rat. The Journal of Physiology, 523 Pt 2(Pt 2), 479–491. 10.1111/j.1469-7793.2000.t01-1-00479.x [PubMed: 10699090]

Stickland NC (1975). A detailed analysis of the effects of various fixatives on animal tissue with particular reference to muscle tissue. Stain Technology, 50(4), 255–264. 10.3109/10520297509117068 [PubMed: 810925]

Stolinski C (1995). Structure and composition of the outer connective tissue sheaths of peripheral nerve. Journal of Anatomy, 186 (Pt 1(Pt 1), 123–130. https://pubmed.ncbi.nlm.nih.gov/7649808 [PubMed: 7649808]

Sweeney JD, Ksienski DA, & Mortimer JT (1990). A nerve cuff technique for selective excitation of peripheral nerve trunk regions. IEEE Transactions on Biomedical Engineering, 37(7), 706–715. 10.1109/10.55681 [PubMed: 2394459]

The Vagus Nerve Stimulation Study Group. (1995). A randomized controlled trial of chronic vagus nerve stimulation for treatment of medically intractable seizures. Neurology, 45(2), 224–230. 10.1212/wnl.45.2.224 [PubMed: 7854516]

Thompson N, Ravagli E, Mastitskaya S, Iacoviello F, Stathopoulou T-R, Perkins J, Shearing PR, Aristovich K, & Holder D (2022). Organotopic organization of the cervical vagus nerve. BioRxiv, 2022.02.24.481810. 10.1101/2022.02.24.481810

Tigerholm J, Petersson ME, Obreja O, Lampert A, Carr R, Schmelz M, & Fransen E (2014). Modeling activity-dependent changes of axonal spike conduction in primary afferent C-nociceptors. Journal of Neurophysiology, 111(9), 1721–1735. 10.1152/jn.00777.2012 [PubMed: 24371290]

Upadhye AR, Kolluru C, Druschel L, Al Lababidi L, Ahmad SS, Menendez DM, Buyukcelik ON, Settell ML, Blanz SL, Jenkins MW, Wilson DL, Zhang J, Tatsuoka C, Grill WM, Pelot NA,

Ludwig KA, Gustafson KJ, & Shoffstall AJ (2022). Fascicles split or merge every ~560 microns within the human cervical vagus nerve. Journal of Neural Engineering 10.1088/1741-2552/ac9643

Uthman BM, Wilder BJ, Penry JK, Dean C, Ramsay RE, Reid SA, Hammond EJ, Tarver WB, & Wernicke JF (1993). Treatment of epilepsy by stimulation of the vagus nerve. Neurology, 43(7), 1338–1345. 10.1212/wnl.43.7.1338 [PubMed: 8327135]

Van Rossum G, & Drake FL (2009). Python 3 Reference Manual. CreateSpace.

Vespa S, Stumpp L, Bouckaert C, Delbeke J, Smets H, Cury J, Ferrao Santos S, Rooijakkers H, Nonclercq A, Raedt R, Vonck K, & El Tahry R (2019). Vagus Nerve Stimulation-Induced Laryngeal Motor Evoked Potentials: A Possible Biomarker of Effective Nerve Activation. Frontiers in Neuroscience, 13, 880. 10.3389/fnins.2019.00880 [PubMed: 31507360]

Weerasuriya A, Spangler RA, Rapoport SI, & Taylor RE (1984). AC impedance of the perineurium of the frog sciatic nerve. Biophysical Journal, 46(2), 167–174. 10.1016/S0006-3495(84)84009-6 [PubMed: 6332648]

Yoo PB, Lubock NB, Hincapie JG, Ruble SB, Hamann JJ, & Grill WM (2013). High-resolution measurement of electrically-evoked vagus nerve activity in the anesthetized dog. Journal of Neural Engineering, 10(2), 26003. 10.1088/1741-2560/10/2/026003

Zannad F, De Ferrari GM, Tuinenburg AE, Wright D, Brugada J, Butter C, Klein H, Stolen C, Meyer S, Stein KM, Ramuzat A, Schubert B, Daum D, Neuzil P, Botman C, Castel MA, D'Onofrio A, Solomon SD, Wold N, & Ruble SB (2015). Chronic vagal stimulation for the treatment of low ejection fraction heart failure: results of the NEural Cardiac TherApy foR Heart Failure (NECTAR-HF) randomized controlled trial. European Heart Journal, 36(7), 425–433. 10.1093/eurheartj/ehu345 [PubMed: 25176942]

Novelty & Significance:

By simulating activation thresholds across human, pig, and rat vagus nerve stimulation, we validated the accuracy of ASCENT across an order of magnitude of nerve diameters, cuff diameters, waveform pulse widths, and fiber diameters. Accounting for individual-specific differences in nerve morphology reproduced observed variability in neural and physiological responses to vagus nerve stimulation.

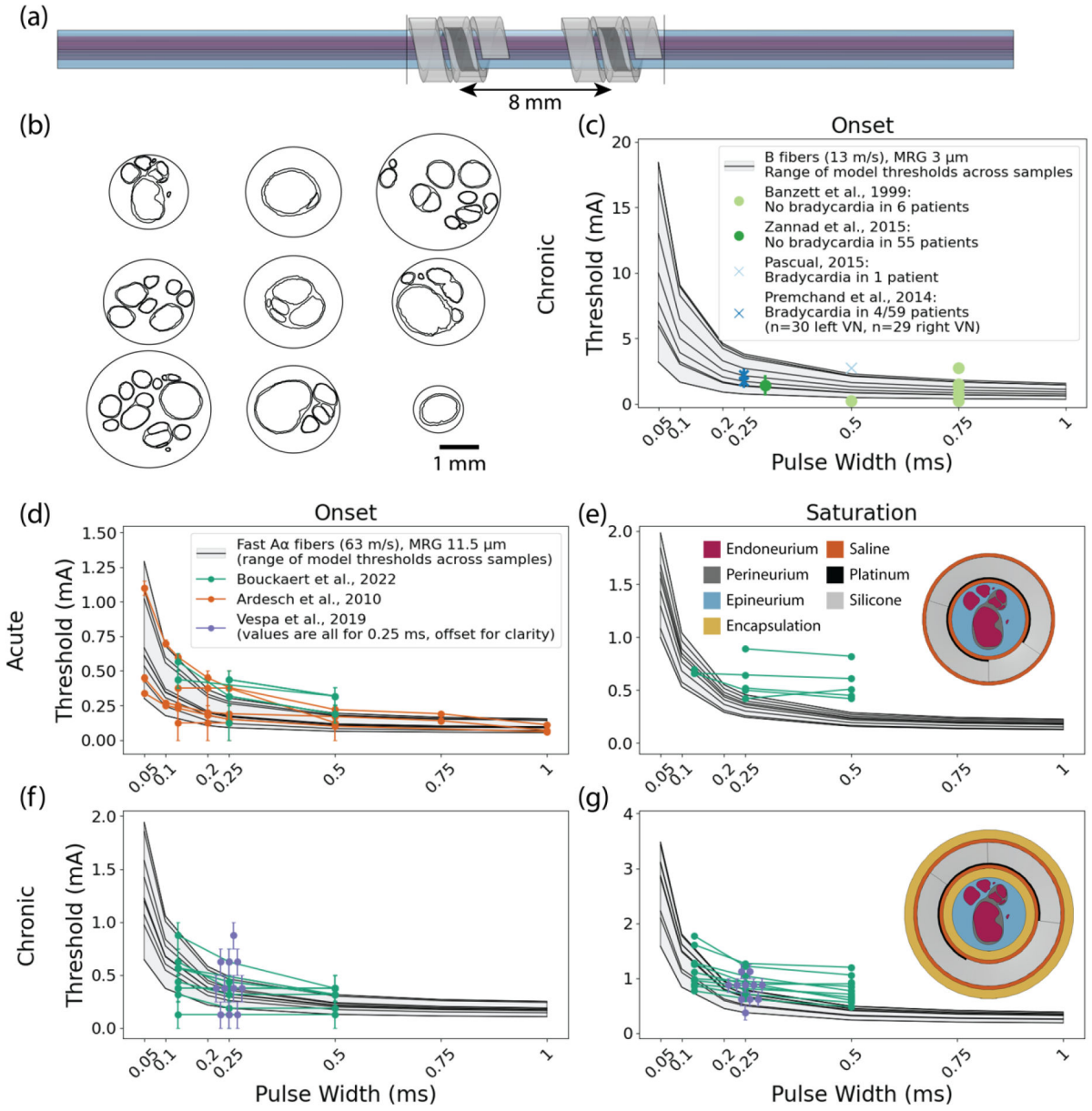

Figure 1.

Comparison of modeled VNS thresholds for human Aα and B fibers to clinical laryngeal EMG and bradycardia thresholds, respectively. (a): Longitudinal view of a finite element model of a human vagus nerve instrumented with the clinical LivaNova bipolar helical cuff electrode. (b): Cross sections of human vagus nerves modeled from (Pelot et al., 2020c, 2020a). (c): Strength-duration data for B fiber thresholds in nine chronic human VNS models (shaded region). Clinical VNS that caused bradycardia (blue “x”) or no bradycardia (green “o”). (d): Strength-duration data for onset of laryngeal EMG responses in acutely implanted patients (Ardesch et al., 2010; Bouckaert et al., 2022) and modeled Aα fiber activation thresholds. Legend applies for (d)-(g). (e): Strength-duration data for saturation of laryngeal EMG responses in acutely implanted patients (Bouckaert et al., 2022) and modeled Aα fiber activation thresholds. The inset provides an example cross

section of modeled acute human VNS to show the materials of the nerve and cuff; the color legend defines the FEM materials in panels (a), (e), and (g). (f): Strength-duration data for onset of laryngeal EMG responses in chronically implanted patients (Bouckaert et al., 2022; Vespa et al., 2019) and modeled Aα fiber activation thresholds. (g): Strength-duration data for saturation of laryngeal EMG responses in chronically implanted patients (Bouckaert et al., 2022; Vespa et al., 2019) and modeled Aα activation thresholds. The inset provides an example cross section of modeled chronic human VNS to show the materials of the nerve and cuff. See Supplemental Figure 1 in Appendix 5 for modeled activation thresholds for smaller-diameter Aα fibers. See Supplemental Figure 2 in Appendix 5 for strength-duration data for each fascicle in each acute human model. All (Vespa et al., 2019) data are for a pulse width of 0.25 ms, but were offset along the x axis for visual clarity. The error bars in (c) represent standard deviation. The error bars in (d)-(g) represent the amplitude step sizes used clinically; the top and bottom of each error bar is defined by the lowest amplitudes tested experimentally that evoked an EMG response and the next lowest amplitude, respectively, and the data point marks the mean. Some error bars in (Ardesch et al., 2010) are not visible due to the small step sizes used experimentally. The saturation thresholds from (Bouckaert et al., 2022) are from Boltzmann fits to the experimental data (95% V_{max}) and therefore do not have error bars.

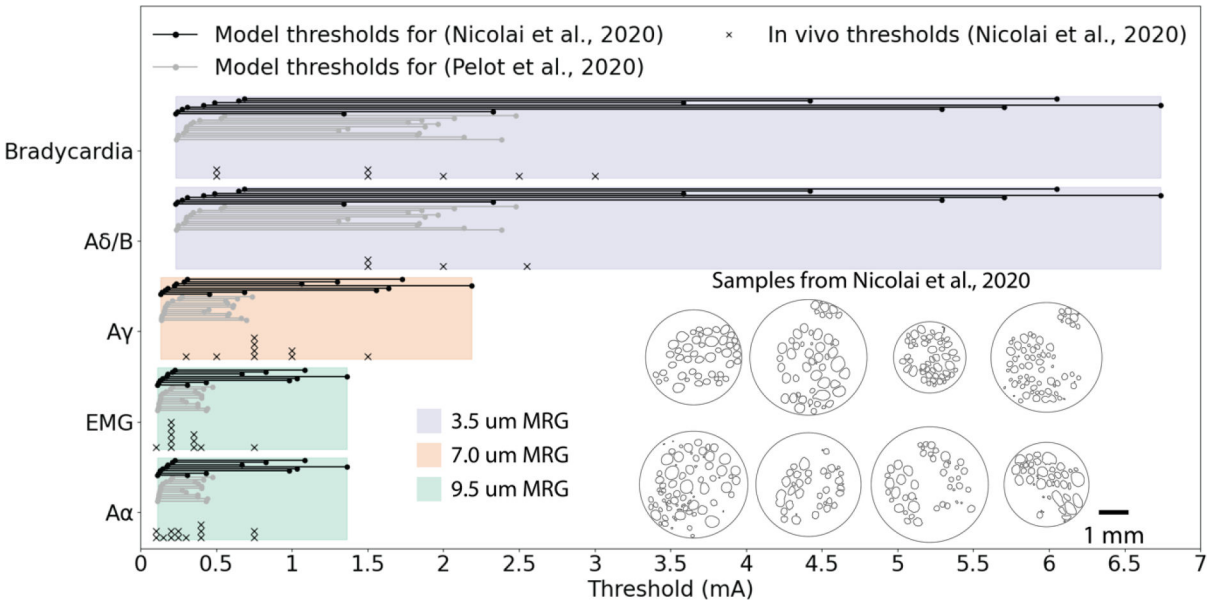

Figure 2.

Comparison of modeled and in vivo pig VNS thresholds. We modeled fiber diameters (Table 2; color legend) corresponding to the recorded compound action potential fiber types (Aα, Aδ/B,, and Aγ fibers) and physiological signals (laryngeal EMG and bradycardia) (Nicolai et al., 2020, 2021; Settell et al., 2023). We used a 0.2 ms/phase biphasic symmetric rectangular pulse with no inter-phase delay to match the waveform used in vivo. The inset shows cross sections of 8 pig vagus nerves (Settell et al., 2023), corresponding to the animals for which we have threshold data (black x's) (Nicolai et al., 2020, 2021). Additional cross sections for 12 pigs from (Pelot et al., 2020c, 2020b) are shown in Supplemental Figure 7f in Appendix 8.

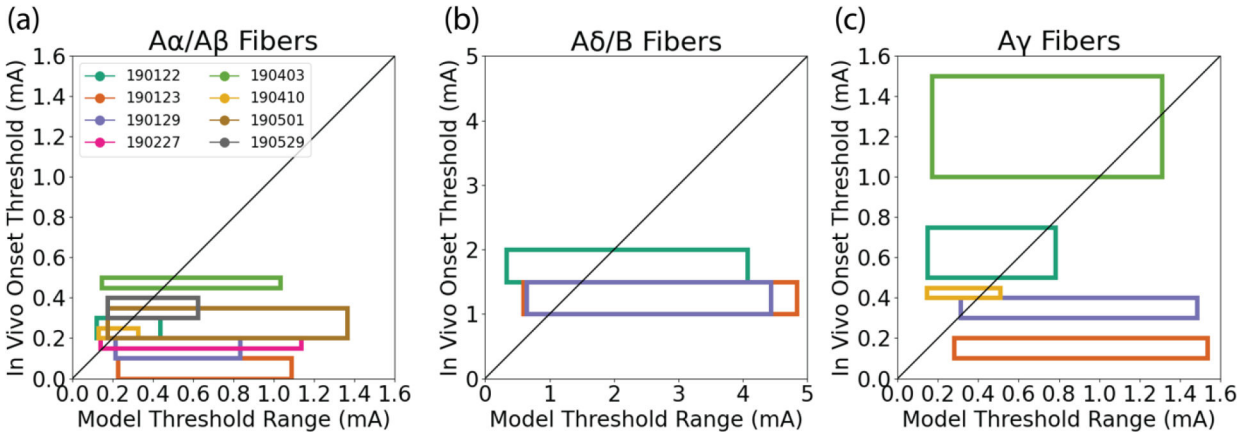

Figure 3.

In vivo onset and modeled thresholds using fiber diameters chosen for each animal to match the mean CV across CAP signals collected (Supplemental Table 2 in Appendix 8). The width of each box was defined by the minimum and maximum model fiber thresholds across all fascicles, which accounts for uncertainty in location of fascicles that contain the fibers which produced the recorded response. The top and bottom of each box is defined by the amplitudes tested in vivo that first produced CAP response and the next lowest amplitude (i.e., did not produce discernable response), respectively. We used a 0.2 ms/phase biphasic symmetric rectangular pulse with no inter-phase delay to match the waveform used in vivo.

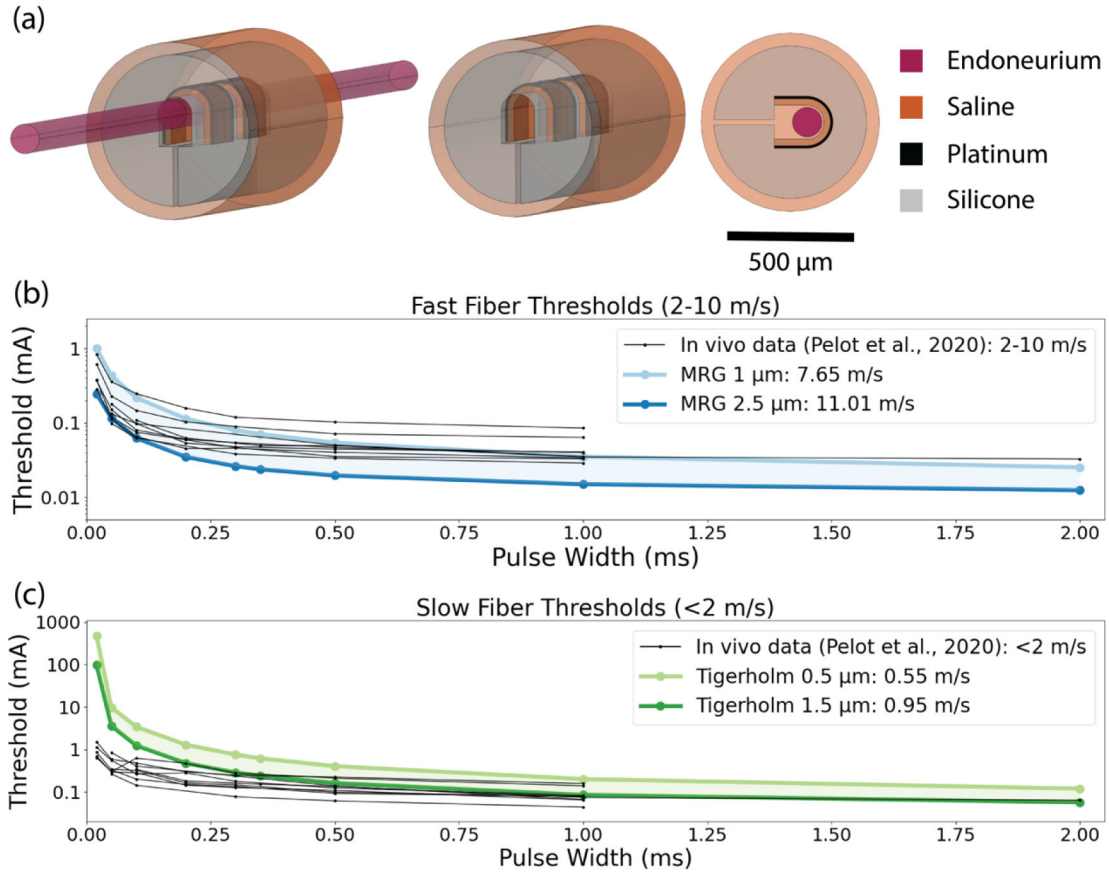

Figure 4.

Model of rat cervical VNS compared to published in vivo recordings ($n = 9$) (Pelot & Grill, 2020). (a): Finite element model geometry of a 235 µm diameter nerve in the 300 µm Micro-Leads cuff. (b): Strength-duration data for "fast" fibers with conduction responses at >2 m/s, modeled as small, myelinated fibers. (c): Strength-duration data for "slow" fibers with conduction responses at <2 m/s, modeled as unmyelinated fibers.

Table 1.

Material conductivities used in finite element models of VNS.

Material	Electrical Conductivity σ (S/m)	References
Muscle	{0.086, 0.086, 0.35}	(Gielen et al., 1984)
Silicone	10^{-12}	(Callister & Rethwisch, 2012)
Platinum	9.43×10^{6}	(de Podesta et al., 1996)
Saline	1.76	(Horch, 2017)
Encapsulation Tissue	0.159	(Grill & Mortimer, 1994)
Epineurium	0.159	(Grill & Mortimer, 1994; Pelot et al., 2017; Stolinski, 1995)
Perineurium	0.0008703	(Pelot et al., 2019; Weerasuriya et al., 1984)
Endoneurium	{0.167, 0.167, 0.571}	(Pelot et al., 2019; Ranck & BeMent, 1965)

Table 2.

Fiber models and diameters to simulate VNS-evoked neural and physiological responses in humans, pigs, and rats. The third column indicates if the fiber model was chosen from experimental CV (i.e., mean CV value from recorded signals or the high/low cutoff CV used to ascribe neural signals to fiber types) or from published distribution of fiber diameters.

Species	Fiber Type	CV Determination: Recorded Mean Cutoff (Low or High) Diameter Distribution	Experimental CV (m/s)	Published Diameter (μm)	Fiber Model and Diameter	Modeled CV (m/s)
Human	Aα	Cutoff Low	30.5 (Ardesch et al., 2010)	-	MRG 6.5 μm	31.3
Human	Aα	Cutoff High	62.8 (Ardesch et al., 2010)	-	MRG 11.5 μm	63.2
Human	B	Diameter Distribution		3 (Guo et al., 1987; Schnitzlein et al., 1958)	MRG 3 μm	13.1
Pig	Aα/Aβ	Recorded Mean	49.79 (Nicolai et al., 2020)	-	MRG 9.5 μm	50.8
Pig	Aα	Cutoff Low	70 (Nicolai et al., 2020)	-	MRG 12.5 μm	70.1
Pig	Aα	Cutoff High	120 (Nicolai et al., 2020)	-	MRG 16 μm	90.7
Pig	Aβ	Cutoff Low	40 (Nicolai et al., 2020)	-	MRG 8 μm	41.1
Pig	Aβ	Cutoff High	70 (Nicolai et al., 2020)	-	MRG 12.5 μm	70.1
Pig	Aγ	Recorded Mean	33.93 (Nicolai et al., 2020)	-	MRG 7 μm	34.6
Pig	Aγ	Cutoff Low	15 (Nicolai et al., 2020)	-	MRG 3.5 μm	15.3
Pig	Aγ	Cutoff High	40 (Nicolai et al., 2020)	-	MRG 8 μm	41.1
Pig	Aδ/B	Recorded Mean	14.76 (Nicolai et al., 2020)	-	MRG 3.5 μm	15.3
Pig	Aδ	Cutoff Low	5 (Nicolai et al., 2020)	-	MRG 1 μm	7.65
Pig	Aδ	Cutoff High	15 (Nicolai et al., 2020)	-	MRG 3.5 μm	15.3
Pig	B	Cutoff Low	3 (Nicolai et al., 2020)	-	MRG 1 μm	7.65
Pig	B	Cutoff High	14 (Nicolai et al., 2020)	-	MRG 3 μm	13.1
Rat	“Fast”	Cutoff Low	2 (Pelot & Grill, 2020)	-	MRG 1 μm	7.65
Rat	“Fast”	Cutoff High	10 (Pelot & Grill, 2020)	-	MRG 2.5 μm	11.0
Rat	“Slow”	Cutoff Low	0.5 (Pelot & Grill, 2020)	-	Tigerholm 0.5 μm	0.55
Rat	“Slow”	Cutoff High	2 (Pelot & Grill, 2020)	-	Tigerholm 1.5 μm	0.95